Back-projection imaging of a tsunami excitation area with ocean-bottom pressure gauge array data

Ayumu Mizutani[1], Kiyoshi Yomogida[2]

[1]Department of Natural History Science, Graduate School of Science, Hokkaido University, Sapporo 060-0810, Japan

[2]Department of Earth and Planetary Science, Faculty of Science, Hokkaido University, Sapporo 060-0810, Japan

Key Points:

- The back-projection analysis is applied to tsunami records of an OBPG array associated with the 2016 Off-Fukushima earthquake.
- Back-projection images represent not only an excitation area but also detect a part of the feature of early tsunami propagations.
- Our back-projection result suggests that the fault size of this earthquake was about half of the standard scaling law.

Corresponding author: A. Mizutani, `a_mizutani@frontier.hokudai.ac.jp`

Abstract

A back-projection method has been applied to many earthquakes in seismology due to its simple and low computational cost, and it can estimate complex fault rupture processes without any specific a priori information. In this study, we applied the back-projection method to the tsunami records observed by an ocean-bottom pressure gauge array and demonstrated it to be a powerful new tool other than the familiar waveform inversion. The obtained back-projection image was consistent with the initial tsunami height distributions estimated by previous waveform inversions, and its spatial resolution appeared to be even better. Our result suggests that the fault size of the 2016 Off-Fukushima earthquake was about half, different from the scaling law of standard earthquakes. The present tsunami back-projection analysis can also estimate the feature of early tsunami propagations. In addition, the estimated image seems to be reliable even 30 min after the origin time, so the back-projection analysis will be useful in an early detection of the location and spatial extent of a tsunami source. In the present case, the number of available stations in the analysis was found to be affected by the diffraction of tsunami propagation caused by the refraction by a high velocity zone near the Japan trench. In other words, the further the source is from the coast, the more stations to be analyzed are available. Since most tsunami-generating earthquakes occur near the subduction axis or its outer-rise region, the back-projection analysis should be effective for source estimation of the majority of tsunami-generating earthquakes.

Plain Language Summary

In seismology, the back-projection method has been applied to many earthquakes to retrieve their source processes. The operation of the back-projection analysis consists of a simple stacking of the waveforms shifted with each travel time from a target area. The key points of the back-projection analysis are therefore the number of stations and accurate travel time estimation. Ocean-bottom pressure gauge (OBPG) arrays have been recently developed around the world, and the bathymetry or its corresponding tsunami travel time is known much better than the Earth's internal structure. This study is the first attempt to apply the back-projection method to the tsunami records observed by an OBPG array. We found that the tsunami source area estimated by the back-projection has better resolution than a waveform inversion technique, a popular source estimation method. It was also revealed that the tsunami back-projection analysis estimates not only the tsunami source but also an early stage of tsunami propagations. Because the back-projection analysis requires low computational cost, it should be complementary to current tsunami early warning systems. The back-projection analysis could be an important tool for the tsunami source estimation in the new era of ocean-bottom array observatories.

1 Introduction

Ocean-bottom pressure gauge (OBPG) arrays have been recently deployed around the world. These arrays enable us to observe tsunamis propagating across such an array directly. Tsunami recordings by an OBPG array have been analyzed by various approaches: for example, to estimate tsunami source processes (e.g., Kubota, Kubo, et al., 2021; Fukao et al., 2018; Hossen et al., 2015), to reconstruct tsunami wavefields by data assimilation (e.g., Gusman et al., 2016; Wang & Satake, 2021), to detect scatterers of tsunami waves by the beamforming method (Kohler et al., 2020), and to derive a phase velocity map of tsunamis by the eikonal tomography (Lin et al., 2015).

In seismology, the back-projection analysis is known to be a relatively new but powerful array-based method to image the rupture process of large earthquakes (e.g., Ishii et al., 2005; Yagi et al., 2012). This approach utilizes the seismograms recorded at a dense seismic network or array. There are two major advantages of this method over conventional and popular waveform inversion approaches (e.g., Kiser & Ishii, 2017): (1) It requires minimal a priori constraints, that is, we do not need information such as the geometry and location of a finite fault plane. (2) Its basic operation is only to stack the seismic records shifted by each theoretical travel time, so that the massive and generally unstable calculation of inverted matrices in inversion methods is not required. These advantages enable the back-projection method to require small computation cost to obtain a reliable result. On the other hand, because of its simplicity, the physical justification of the back-projected image has not been fully established yet. In seismology, it is considered that the back-projection image represents the seismic energy release on a fault plane (e.g., Ishii et al., 2005). Fukahata et al. (2014) clarified several theoretical aspects of the back-projection method, pointing out that the key condition for its appropriate performance is the stack of Green's functions for all the stations close to the delta function both in time and space domains. Note that the Green's functions are not used in the present back-projection analysis although they are related to its performance.

In this paper, we applied the back-projection method to, not seismograms, but tsunami waveforms recorded by an OBPG array, called the Seafloor Observation Network for Earthquakes and Tsunamis along the Japan Trench (S-net) off the northeastern coast of Japan (e.g., Aoi et al., 2020). In the case of tsunamis, under the linear long-wave approximation for short travel distance, the phase speed c can be represented as $c = \sqrt{gh}$, where g is the gravitational acceleration and h is the sea depth. The sea depth at every location is known much better than the Earth's internal structure for seismic data, so that we can make much more accurate travel time corrections than in the case of seismic waves although the spatial variation of tsunami velocities is more complex and stronger than the seismic case in general. The back-projection imaging of tsunamis is therefore expected to yield more satisfactory results than that of previous seismic-wave studies. Note that the tsunami back-projection in this study focuses on the tsunamis generated inside or near an array, while most of the seismic back-projections have utilized teleseismic P-waves or applied to the earthquake outside or far from an array.

Another advantage of the tsunami back-projection is that it will be useful for tsunami early warning. The source mechanism of tsunamis is often estimated as a solution to a given linear inverse problem (e.g., Satake, 1987; Saito et al., 2010; Tsushima et al., 2012). To solve the inverse problem, we need several pieces of the source information a priori estimated from seismic data. As mentioned above, the back-projection can estimate an excitation area without any knowledge of a priori fault geometry information and extensive computational cost. A back-projection result should be thefore suitable to get a prompt and reliable estimation of the tsunami source for tsunami early warning.

A time-reversal imaging is another imaging approach to characterize earthquake sources based on the time-reversed (i.e., $t \rightarrow -t$) wave equation (e.g., Larmat et al., 2006). Several studies have applied a time-reversal imaging technique to the tsunami records (e.g., Hossen et al., 2015; An & Meng, 2017). Nevertheless, solving the wave equation requires more computational cost than the simple stack of the back-projection analysis, so that the back-projection analysis would be more practical for tsunami early warning.

This study applied the back-projection analysis to the tsunami data recorded by the OBPG array, checking what a tsunami back-projection image really represents, and confirmed its applicability for tsunami early warning. Section 2 explained the OBPG data in the present analysis and formulated a back-projection method suitable for tsunami data. In Section 3, some important characteristics of the tsunami back-projection analysis were investigated with numerical experiments. Next, we confirmed that the tsunami back-projection of the S-net indeed satisfies the condition derived by Fukahata et al. (2014) in Section 4, and then applied it to real data in Section 5. We also evaluated our back-projection image in comparison with the results of previous studies and numerical experiments. In Section 6, we investigated the potential of the back-projection analysis for tsunami early warning. Section 7 interpreted the obtained results and investigated other possible tsunami-generating events.

2 Data and Method

In this study, we applied the back-projection analysis to the OBPG records of S-net associated with the 2016 Off-Fukushima earthquake (M_w 6.9). The tsunami waves generated by this earthquake is the largest that has ever occurred around Japan island since the first operation of S-net in 2013. S-net is a real-time cabled ocean-bottom observation network deployed off eastern Japan in the Pacific Ocean (e.g., Aoi et al., 2020). The main framework of the S-net stations consists of seismometers and OBPGs at each station, and stations are connected with cables to the monitoring base on land for real-time observations.

S-net consists of 150 stations as its final form in the present, however, 25 stations located in an outer-trench region were not installed when this event occurred. Station S2N13 which was located just above the focal area, did not record any pressure changes because the pressure observation component of this station appears not to have worked correctly (Kubota, Kubo, et al., 2021).

As preliminary data corrections, we first removed both ocean tide and DC components from the original OBPG records, that is, we set the average of each record to be zero. We subtracted the theoretical tide calculated by the model of Matsumoto et al. (2000), as well as the average of each OBPG record in 1 minute before the earthquake as its DC component. Note that the DC component is originated from the deployment ocean depth of each station. Then, a band-pass filter of 100 – 3000 sec was applied to extract tsunami components. The second-order Butterworth filter was applied to both forward and backward in time.

Note that one of the advantages of the back-projection analysis in seismology is to image the temporal and spatial rupture process on a given fault plane, but the tsunami back-projection analysis is not at least in the present case of a small event. This is because the period of tsunamis analyzed is longer than a general rupture duration. That is, the excitation of tsunami is imaged at a single time step, even for an M8-sized earthquake (i.e., the source duration less than 100 sec).

According to the Japan Meteorological Agency (JMA), the 2016 Off-Fukushima earthquake occurred on November 21 at 20:59 UTC. Its epicenter and centroid depth were at 37.36N°, 141.60E°, and 12 km, respectively. This was a very shallow normal fault earthquake in the upper plate of the Japan trench subduction zone and generated small but clear tsunamis observed at several coastal tide gauges and many off-shore S-net OBPG stations for the first time.

Previous studies have estimated the tsunami source mechanism of this earthquake by the waveform inversion approach based on the methodology of Satake (1987), that is, solving a linear inverse problem with the Green's functions of the linearized tsunami propagation. Gusman et al. (2017) and Adriano et al. (2018) mainly used tide gauge records, while Kubota, Kubo, et al. (2021) mainly used S-net OBPG records. All these studies indicated that the main part of its coseismic displacement was subsidence with an amplitude of about 1.3 – 2.4 m. This feature is consistent with the focal mechanism of this normal fault earthquake estimated by seismic data (Nakata et al., 2019).

A back-projection image of records in original seismic studies is expressed as follows (e.g., Ishii et al., 2007):

$$s_l(t) = \sum_{k=1}^{N} w_k d_k(t + t_{kl}^{travel}), \tag{1}$$

where s_l represents the stacked waveform at the lth potential source grid, d_k is the seismic or tsunami waveform observed at the kth station ($k = 1, ..., N$), w_k is the weighting factor for the kth station, and t_{kl}^{travel} is the theoretical travel time between the lth source grid and the kth station, respectively. Candidates of source grids in this study covered the area in longitude between 141E° and 142.5E° and in latitude between 36N° and 38.5N° with the grid spacing of 0.01° in both longitude and latitude (Figure 1(A)). In this study, w_k was defined to normalize each waveform by the maximum of its absolute value because this earthquake occurred inside the S-net coverage area and the am-

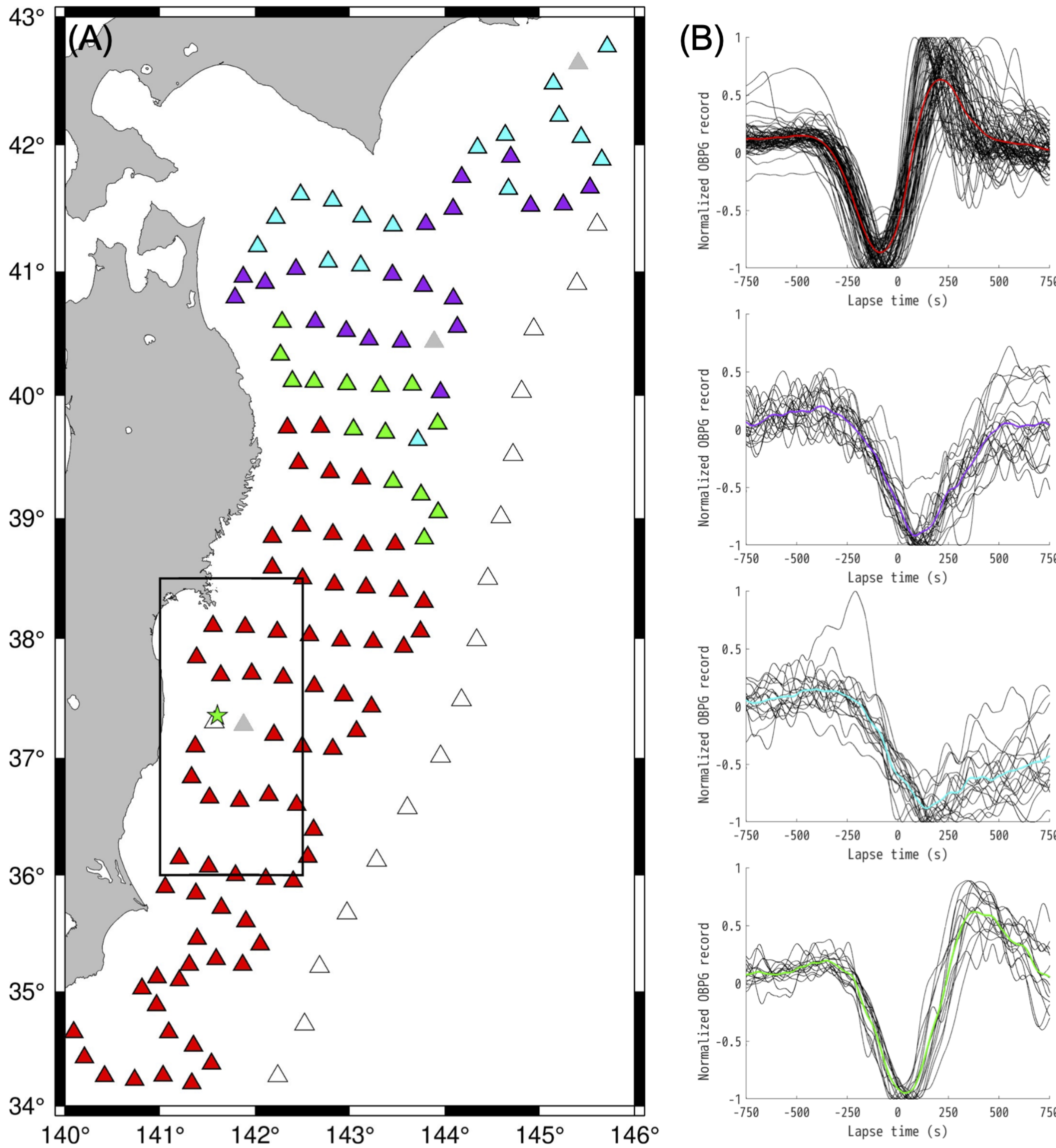

Figure 1. (A) Locations of S-net stations and the target area of the back-projection analysis (the black rectangle). The colors of stations represent the resulting clusters for mutually coherent records. Gray triangles are the stations that do not belong to any clusters, and the stations not available in this study (i.e., S2N13 and the outer-trench stations) are plotted as open triangles. The green star represents the epicenter of the 2016 Off-Fukushima earthquake. (B) Tsunami records of all the stations for each cluster. Red, purple, cyan, and green lines represent the average waveforms, and each color corresponds to the cluster in (A). The lapse time of zero is set from each theoretical travel time.

plitude difference between near- and far-field stations was about 35 times. Each theoretical travel time t_{kl}^{travel} was calculated by the Fast Marching Method (FMM; e.g., Sethian, 1999). The FMM is an algorithm to solve the eikonal equation in space numerically, and a stable travel time connecting any source-station pair can be obtained even if the phase speed contrast in a medium is strong. The phase speed map for the FMM was defined as $\sqrt{gh}$, i.e., the travel time under the linear long-wave approximation. Since we filtered the data in a period of longer than 100 sec, this non-dispersive assumption should affect the resulting images little. As the bathymetry data, we used the ETOPO1 (Amante & Eakins, 2009), and travel times were calculated for the oceanic area in depth deeper than 100 m to avoid complex propagation effects near coasts.

Since the back-projection analysis stacks waveforms based on theoretical travel times, the size of travel time errors might affect the final result. The travel time and its error between two grid points can be expressed as $\Delta t = \Delta x/\sqrt{gh}$ and $\Delta t - \Delta t_{err} = \Delta x(1/\sqrt{h} - 1/\sqrt{h_{err} + h})/\sqrt{g}$, where h_{err} is the bathymetry error and Δt_{err} is its corresponding error in travel time. At least, the bathymetry data of this region adopted in this study have sufficient horizontal resolution, considering the 500 m mesh data around Japan (Amante & Eakins, 2009). In addition, even if the bathymetry error were twice as the actual bathymetry in the worst case, the travel time error should not exceed 10 seconds. Compared with the analyzed period range (¿ 100 sec), the theoretical travel times used in this study should be sufficiently reliable.

In the final step, the tsunami back-projection image was given by:

$$BP_l(t) = \frac{1}{\max\limits_{l}\{BP_l(t)\}} \int_{t-\alpha}^{t+\alpha} \{s_l(\tau)\}^2 d\tau, \tag{2}$$

where $BP_l(t)$ represents the back-projection image at the lth grid and α is the time window for integrating the stacked waveform $s_l(t)$ of Equation 1. We normalized the image by the maximum of all the grids at each time step, $BP_l(t)$. In this study, α was defined as 150 seconds, and $t = 0$ was the earthquake origin time estimated using the seismic records by JMA. Note that the earthquake origin time can be estimated before the back-projection analysis because the seismic wave speed is much faster than the tsunami one. In other words, even in the case of tsunami early warning, the information of the origin time can be assumed to be available.

The essence of the back-projection method is to stack coherent waveforms among stations, so that a kind of cluster analysis was conducted in order to group stations with waveforms resembling each other (Ishii et al., 2007). We conducted a hierarchical cluster analysis (Romesburg, 2004) with the correlation coefficients estimated by the Unweighted Pair-Group Method using arithmetic Averages (UPGMA) to the normalized waveforms $w_k d_k$ of Equation (1). The correlation coefficient was calculated for each pair of waveforms in the time window of 750 seconds before and after each theoretical travel time. The theoretical travel time was calculated assuming that the source location was the same as the Global CMT (GCMT) solution (37.31N°, 141.46E°). The cluster tree obtained by this analysis was truncated with a correlation coefficient of 0.6, that is, the correlation coefficients of records belonging to each group to be larger than 0.6. Figure 1 shows the result of the present cluster analysis. In the following back-projection analysis, we only used the data of the stations belonging to the largest cluster, that is, 70 stations in red of Figure 1.

Figure 2 shows a schematic view of each step in the proposed method. Although an original OBPG record may contain non-tsunami components such as seismic waves especially in a coseismic time window, particularly at stations close to the source (e.g., Saito & Tsushima, 2016; Mizutani et al., 2020), such effects on the back-projection analysis should be minor because of the applied band-pass filter of 100 − 3000 sec and the above cluster analysis to select only coherent signals among stations.

In general, a back-projection analysis estimates only the tsunami image of relative amplitude at each time step because of the normalization process for both each waveform and the back-projection image (Equations 1 and 2). Hossen et al. (2015) estimated the initial tsunami height from their time-reversal image, S_{TRI}. They introduced a scaling factor C for the least-squares minimization of the difference in the maximum value between synthetic (i.e., obtained by the forward propagation of S_{TRI}) and observed waveforms at each station. They found that the initial tsunami heights could be estimated as $C \times S_{TRI}$. In this study, we estimated absolute tsunami heights from the back-proejction image using the same scheme as Hossen et al. (2015). We used the area of $BP(0) > 0.6$ as the synthetic tsunami source. This threshold of 0.6 was selected by a trial-and-error approach to an effective tsunami source area for the reference of the previous studies. Note that all the estimated amplitudes were positive values in our case because both the scaling factor C and the back-projection image $BP(t)$ were positive.

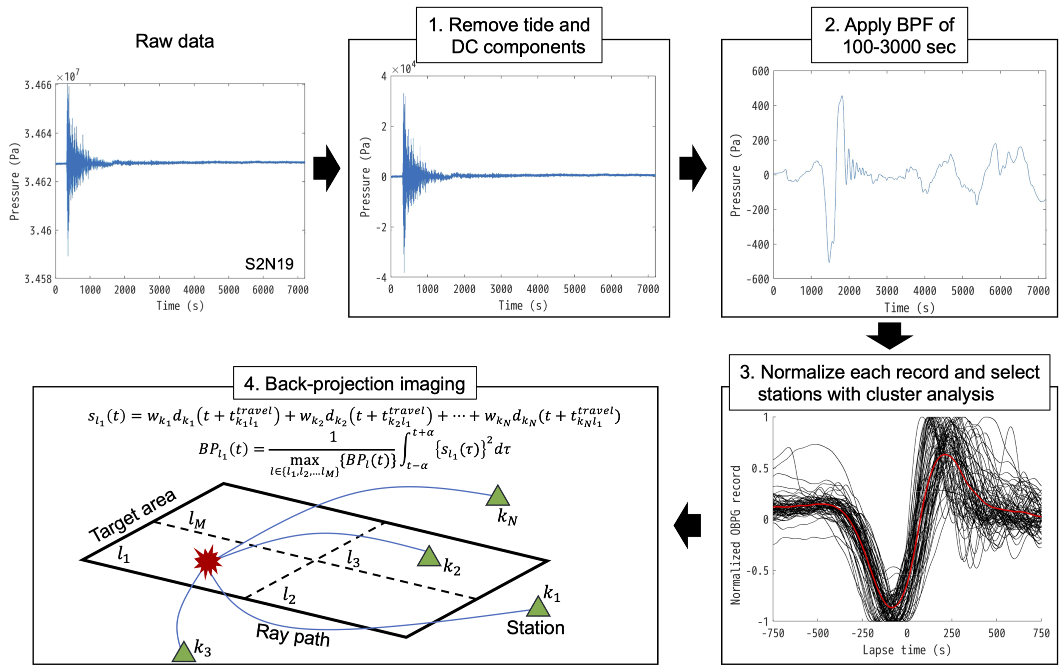

Figure 2. Schematic view of the proposed method. The reference time $t = 0$ in Raw data, Step 1, and Step 2 is 20:55 UTC. The waveforms in Step 3 are those of the red cluster in Figure 1(A). The green triangles, blue lines, and red splash in Step 4 represent the stations, ray paths, and potential source location, respectively.

To evaluate the goodness of the obtained back-projection image, we used the variance reduction (VR) (e.g., Kubota, Suzuki, et al., 2018) defined as:

$$VR = \left(1 - \frac{\sum_k \int [d_k^{obs}(t) - d_k^{syn}(t)]^2 dt}{\sum_k \int [d_k^{obs}(t)]^2 dt}\right) \times 100 \quad (\%), \tag{3}$$

where $d_k^{obs}(t)$ and $d_k^{syn}(t)$ are the observed and synthetic tsunami waveforms at the kth station, respectively. The synthetic waveforms were calculated by the JAGURS code (Baba et al., 2016). The time window for the VR calculation was 400 seconds before and after each theoretical travel time. As the source of the synthetic tsunami waves, the back-projection image with an amplitude greater than 0.6 was multiplied by $-C$, that is, $-C\times BP(0)$, a negative value representing ocean-bottom subsidence for this earthquake (e.g., Gusman et al., 2017).

3 Numerical experiments for the evaluation of tsunami back-projection

In this section, we shall investigate the performance of the present tsunami back-projection analysis with several numerical experiments. In the experiments, we set up

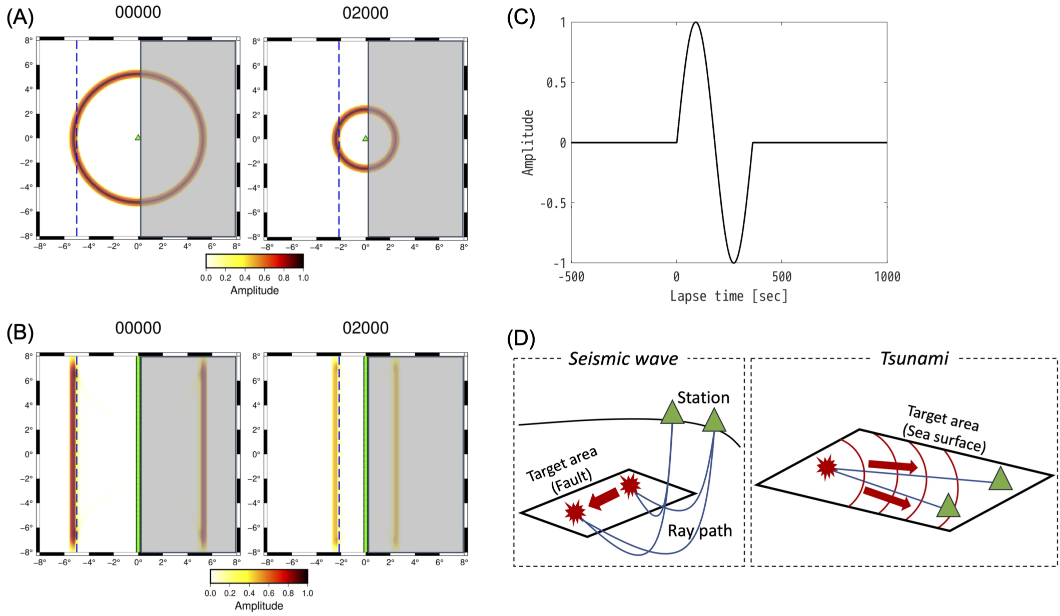

Figure 3. Numerical experiments for the back-projection image of a plane wave source at 0 and 2000 sec. (A) A single station (the green triangle) is located at (0,0) and the blue dashed line represents the assigned plane wave. Note that the amplitudes of the images are normalized at not each time step but $t = 0$ in this case. (B) Same as (A) except for 161 stations located parallel to the plane wavefront. There is a mirror plane-wave image in the shaded area due to the symmetrical setting of this experiment. (C) Synthetic waveform for the plane wave case. Lapse time of 0 means the initial time of the calculation. (D) Schematic figures comparing back-projection analyses with seismic waves and tsunamis. The green triangles, blue lines, and red splashes represent the stations, ray paths, and imaged sources moving in time, respectively.

a constant bathymetry of 2000 m with a grid size of 0.1° or 10 km. Three types of wave sources were prepared: a plane wave, a single Gaussian source, and a dipole source.

Figures 3(A) and 3(B) show the back-projection images for the plane wave case. In this case, a single sinusoidal wave (Figure 3(C)) propagats from left to right. Note that we normalized the back-projection image $BP_l(t)$ by not $\max_l\{BP_l(t)\}$ but $\max_l\{BP_l(0)\}$ only in Figures 3(A) and 3(B), unlike the explanation in Section 2 for real data, to show what the time-lapse back-projection image reflects clearly.

A single station case of Figure 3(A) corresponds to a simple back-projection from the station backward in time, so the images are indeed circular. This result explains what factor reduces the amplitude of the back-projected images in time or distance in the following cases of many stations. The closer to the station, the larger the curvature of the back-projection image. In Figure 3(B) 161 stations are aligned at $x = 0$ with 0.1° intervals. Even without any causes of attenuation such as the geometrical spreading or bathymetry change, the amplitude of the back-projection images appears to decrease with time. In other words, the imaged temporal change in amplitude does not reflect the absolute tsunami height. The decrease in amplitudes is caused by the finite coverage of stations from the result of Figure 3(A). On the other hand, the image at each time step was located correctly, and its spatial distribution of amplitudes is nearly constant or the image of a plane wave can be retrieved well. That is, we may conclude that the present tsunami back-projection analysis could image the basic feature of tsunami propagation though the amplitude can not be compared to that at the other time steps.

Note that there are images in the opposite direction from the stations in Figures 3(A) and 3(B) because the stations are aligned straightly and the bathymetry is constant (i.e., the same travel time at $x < 0$ and $x > 0$). The S-net stations are distributed rather randomly and the bathymetry in and around the target area generally has strong contrast, so such a false mirror image should not exist in the present actual case.

Figures 4(A2) – (A5) show the back-projection images for a single point source of Gaussian spatial distribution. We used a 2-dimensional Gaussian function of the average and the standard deviation of both x and y to be 0 and 50 km with the maximum amplitude of 10 m, i.e.,$10 \times \exp[-(x^2 + y^2)/(2 \times 50^2)]$. The number of stations is the same in all the cases, 90, to investigate the effect of station coverage in three cases: 360°, 180° and 90°. In other words, the stations are two and four times denser in Figures 4(A4) and 4(A5) than 4(A2) and 4(A3), respectively.

Figures 4(A2), 4(A4), and 4(A5) show the back-projection images at t=0 with different coverages of stations. Figure 4(A3) is the same as Figure 4(A2) except the image using a small tsunami source of 1/10 amplitude (i.e., 1 m). Each back-projection image is normalized by each maximum value. From these figures, we may conclude that the source can be successfully estimated if the coverage of stations is more than half or 180° around the source. When stations cover only by 90° (Figure 4(A5)), an isolated image may not be obtained at the correct location and there are several ghost images. Since the utilized S-net stations covered the eastern half of the epicenter in this study (Figure 1), like Figure 4(A4), we confirmed that the back-projection images to be shown and discussed in this study were sufficiently reliable and stable, particularly at their location.

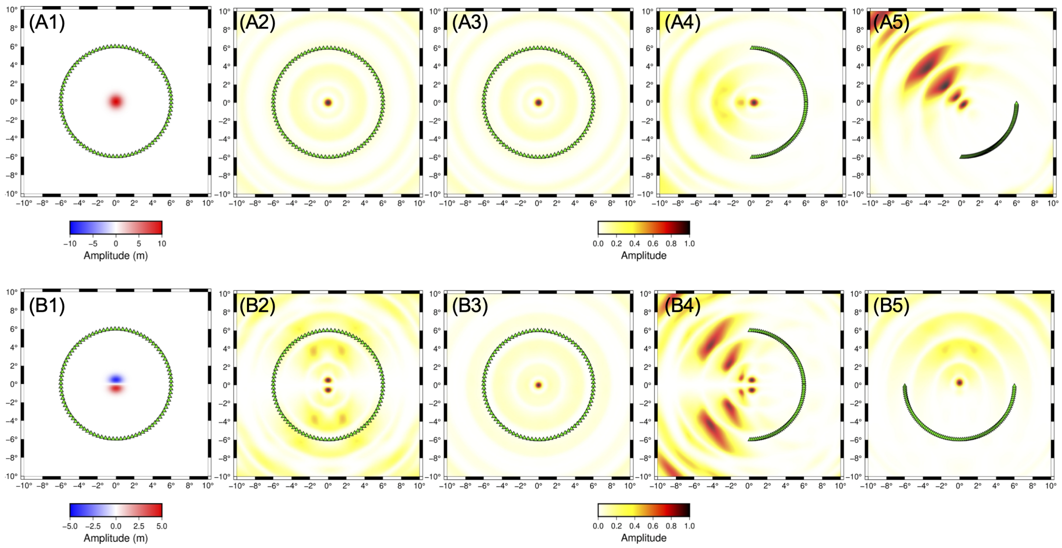

Figure 4. Same as Figure 3 except for a single Gaussian and a dipole source with several radius coverages of stations. (A1) The distributions of the source and stations for (A2) to (A5). The green triangles represent the stations. Note that the source smaller than the others by 1/10 was used for (A3). (A2) – (A5) The back-projection image at $t = 0$. Note that the amplitude is normalized at each figure. (B1) A dipole source for (B2) – (B5). (B2) – (B5) Same as (A2) – (A5) except that the (B1) tsunami source. Note that (B3) was estimated after the correction of polarity.

Next, we investigated the relationship of the amplitude obtained by the present back-projection analysis with the absolute size of tsunami heights. Figures 4(A2) and 4(A3) for large and small tsunami sources not only show the same visual image but also have the same absolute value even before normalizing their images. This is because we normalized each waveform before stacking (Figure 2), that is, $w_k d_k$ in Equation 1 were set to be common regardless of the given source intensity. The difference in the intensity of tsunami sources, therefore, should not affect the obtained image in the normalized procedure of the present back-projection analysis. Since we know a precise velocity model for tsunami propagations, this conclusion should hold even for real data.

We then searched for a supplementary procedure to estimate the absolute amplitude of the tsunami source with the present tsunami back-projection analysis using the scaling factor estimation of Hossen et al. (2015) referred to in Section 2. From the back-projection image of Figures 4(A2) and 4(A4), the estimated amplitudes or the scaling factors C of Hossen et al. (2015) were 7.30 m and 7.47 m, respectively. This means that the amplitude of the obtained image does not largely depend on the angle of station coverage. Meanwhile, we must take care of the difference between the absolute amplitude estimated by the back-projection image and the assinged Gaussian source of 10 m. That is, the present analysis appears to obtain the initial tsunami source height at the source region, or the scaling factor C, underestimated by about 70%, although this number appears to be stable by the condition of observations. This underestimation may be caused by the band-pass filter applied before stacking (Section 2) because the ratio of maximum amplitudes between raw and filtered data was 0.63 on average in this numerical experiment. Since the frequency range of the band-pass filter was determined to extract a tsunami component effectively in this study, our amplitude estimation should reflect the displacement corresponding to tsunami generation. In summary, compared with synthetic and recorded tsunami waveforms at several selected stations, we may estimate even the absolute values of tsunami heights at the source without significant errors.

In the end, we examined the case of a dipole tsunami source, that is, there are areas of both positive and negative at the source. Figure 4(B1) shows the assigned dipole source, and the obtained images are given in Figures 4(B2), 4(B4), and 4(B5). Figure 4(B3) shows the result with a polarity correction, that is, the sign reversed only for the synthetic records at stations $y > 0$ or in the upper half of the figure to follow the part of negative displacements at the source. Such a polarity correction is often used in the seismic back-projection analysis to improve the correlation of each waveform (e.g., Ishii et al., 2005). In the present case, while two separated sub-areas were imaged correctly without the correction as two positive sources located properly (Figure 4(B2)), a single point source was imaged with the correction (Figure 4(B3)). This implies that the polarity correction is not required for the tsunami back-projection analysis. This is probably because the polarity correction would lose the information on the source (i.e., uplift or subsidence). That is, the cancellation of positive and negative signals recorded at each station through the stacking process should be important to image adjacent uplift and subsidence sources. The polarity correction in the tsunami case appears to enhance the resolution of the image in space in an excessive manner, resulting in an image as compact as possible (i.e., monopole), because of not canceling out but overlapping positive (uplift) and negative (subsidence) signals.

Nevertheless, we must be careful that the station coverage seems to affect the back-projection image more than the former case of a single polarity (Fiugres 4(A4), 4(B4) and 4(B5)). If stations cover only parallel to the dipole vector at the source, the image appears to be degraded due to the false stacking of positive and negative polarity in records

(Figure 4(B4)). Still, a point source can be imaged even if stations are located perpendicular to the dipole vector (Figure 4(B5)), probably because the station distribution makes each record to be the same polarity. Although the complexity of tsunami source distributions does not make a serious problem in this study because the displacement of the 2016 Off-Fukushima earthquake was almost only subsidence (e.g., Gusman et al., 2017), we may need to take care of this factor when applying the back-projection analysis to earthquakes with tsunami source areas of both subsidence and uplift.

4 Conditions for good performance in the back-projection imaging

In the previous section, we investigated the characteristics of the tsunami back-projection analysis referring to several numerical experiments, whether our approach can obtain a reliable image of tsunami heights at a source region. In this section, we shall confirm the conditions for its good performance with the real station distribution and bathymetry from a theoretical point of view. Fukahata et al. (2014) revealed the importance of the followings: (1) waveforms from other than the target source grid l are well canceled out each other and (2) the stacked Green's function becomes as close as the delta function. We checked these conditions in order to confirm the validity of images in this study.

Considering causality, in general, the observed waveform at station k can be written as:

$$d_k(t) = \sum_L (a_L * G_{kL})(t), \tag{4}$$

where a_L is the input at the Lth source grid, G_{kL} represents its impulse response (i.e., the Green's function) at the kth station, and $*$ denotes the convolution in time. By substituting Equation (4) into (1), the lth stacked waveform becomes

$$s_l(t) = \sum_k w_k \sum_L (a_L * G_{kL})(t + t_{kl}^{travel}). \tag{5}$$

The above two key conditions can be expressed in the following representations:

$$\sum_k w_k G_{kL}(t + t_{kl}^{traveltime}) \approx 0 \quad (l \neq L, \forall t), \tag{6}$$

$$\sum_k w_k G_{kl}(t + t_{kl}^{travel}) \approx \delta(t). \tag{7}$$

These equations mean that the back-projection image does not have any smearings in both space and time domains. The sum of L in Equation (5) can be ignored when Equation (6) is satisfied:

$$s_l(t) \approx \sum_k w_k (a_l * G_{kl})(t + t_{kl}^{travel}). \tag{8}$$

When Equation (7) is satisfied, moreover, Equation (5) finally leads to our ideal image:

$$s_l(t) \approx a_l(t). \tag{9}$$

In other words, when the stacked Green's function is similar to the delta function in both space and time domains, the back-projection image would reflect the actual physical phenomenon or excitation area in time and space well. Note that the above conditions are related to the stacked Green's function, but they are not required when applying to actual data (Equations (1) and (2)).

To verify Equations (6) and (7) in the present case, we calculated the Green's functions for the 70 stations that we analyzed, using the JAGURS code (Baba et al., 2016). As a synthetic tsunami source for the Green's function, a two-dimensional Gaussian function with a height of 1 m and a width of 2 km was used, and such sources were distributed inside the target area of this study with 0.1° intervals (i.e., L in Equation (6) to be 278).

Figures 5(B) and 5(C) show the spatial variations of ratios in the horizontal lengths between the back-projection image larger than 0.6 and the assigned source for the Green's function (i.e., 2 km) at each source in the x and y (i.e., north-south and east-west) directions, respectively. For x direction, the ratio around the epicenter is small, about 5, but it is as large as 12 in the southwest region of our target area. On the other hand, the ratio is generally very small in the y direction, about 1 except in a southwest region, implying images of high resolution particularly in the north-south direction.

The large ratios in the x direction compared to the y direction seems to be originated from the station distribution which concentrated on the east side of the source. In addition, the large value in the southwest region seems to involve the bathymetry gradient there (Figure 5(A)), that is, the refraction of tsunami waves should affect the obtained image. Although the image of this study can be said to be reliable near the epicenter, we will discuss the effect of station distribution in Section 7.

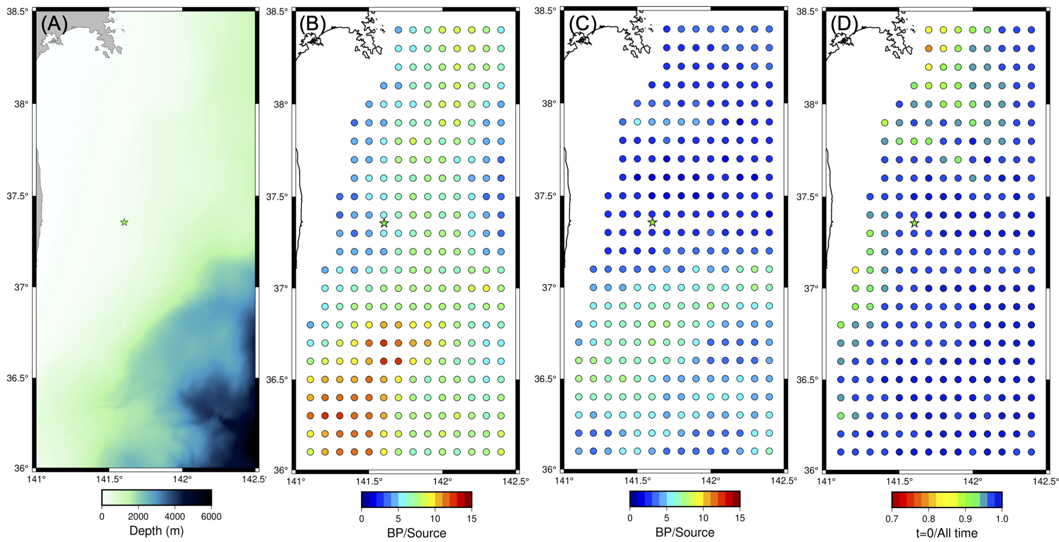

Figure 5. (A) The bathymetry of the target area of this study. The green star represents the epicenter of the 2016 Off-Fukushima earthquake. (B)(C) The horizontal length ratios between the back-projection image of larger than 0.6 and the assigned source for the Green's function (2 km) in the x and y directions. (D) Ratios of the stacked Green's functions integrated in t = -150 – 150 sec and those for each entire record length, i.e., $\int_{-150}^{150}\{s_l(t)\}^2dt/\int_{-\infty}^{\infty}\{s_l(t)\}^2dt$.

Figure 5(D) verifies Equation (7) in this study. Because we integrated the stacked waveforms from -150 to 150 sec for $BP_l(0)$ (Equation 2), we here compared the size of the stacked Green's functions integrated for t = -150 – 150 sec with that for the entire record length, that is,$\int_{-150}^{150}\{s_l(t)\}^2dt/\int_{-\infty}^{\infty}\{s_l(t)\}^2dt$. This ratio would be close to one if Equation (7) is satisfied perfectly. Figure 5(D) shows the condition of Equation (7) seems to be well satisfied at most of the grid points. Values much smaller than one at some points near the coast line may be caused by their small lapse times between each direct and reflected waves. Except for such points, we may say that the back-projection analysis can avoid the effect of reflected waves.

5 Back-projection images using the OBPG array records

In this section, we shall present the results of our tsunami back-projection imaging. The back-projection images here will be compared mainly with the previous result of Kubota, Kubo, et al. (2021) because they estimated initial tsunami heights applying the waveform inversion method to the same S-net OBPG data as this study, which should be superior to other studies with tidal gauge data at coastal stations.

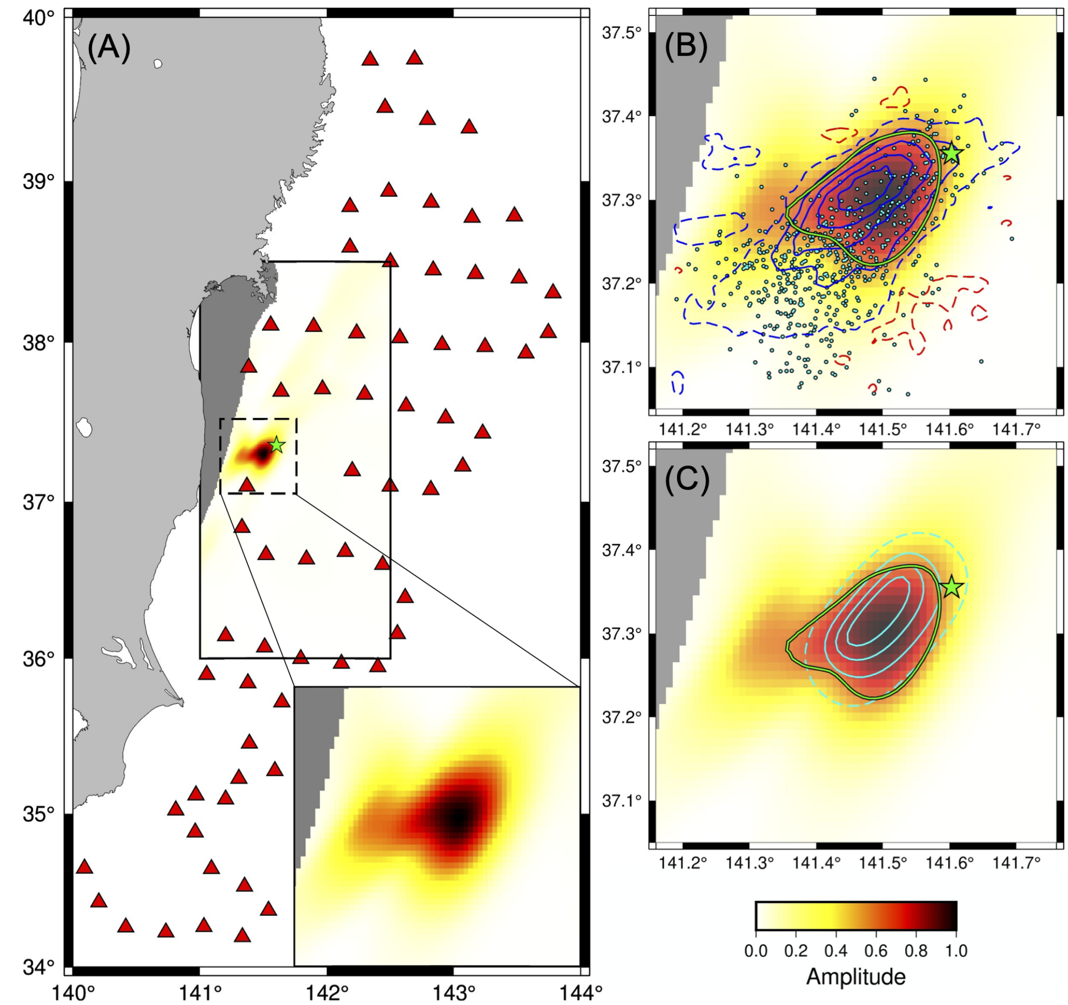

Figure 6. (A) Back-projection image at $t = 0$ or the origin time. The red triangles are the stations used in the analysis. The green star represents the epicenter of the 2016 Off-Fukushima earthquake. The black solid rectangle represents the target area of the back-projection imaging, and the dashed one corresponds to the enlarged area of the right bottom, (B), or (C). (B) Enlarged image of the black dashed rectangle of (A). The green line represents the area with amplitude larger than 0.6. The cyan dots represent the aftershock epicenters. The red and blue contour lines represent the positive and negative amplitudes of the initial tsunami height estimated by Kubota, Kubo, et al. (2021) with the solid to be 0.5 m interval and the dashed to be 0.1 m. Note that there are no solid red contours as the maximum uplift was less than 0.5 m. (C) Same as (B) except that the cyan contour lines represent the subsidence for the single uniform fault slip model of Kubota, Kubo, et al. (2021).

The back-projection imaging at $t = 0$ or the origin time is shown in Figure 6. The obtained image was located not exactly at the epicenter but slightly in the southwest of it. A similar tendency was obtained for the aftershock distribution defined by the earthquakes that occurred shallower than 50 km and within 24 hours after the mainshock. The back-projection image especially is large in the northern part of the aftershock distribution. It is consistent with the region of smaller than -0.5 m (i.e., larger than 0.5 m in amplitude) of the initial tsunami height distribution estimated by the waveform inversion (Figure 6(B)) and the sea-bottom displacement by the grid search of the single fault model (Figure 6(C)) of Kubota, Kubo, et al. (2021). With tidal gauge data, Gusman et al. (2017) and Adriano et al. (2018) also subsided regions, but they were were larger than the one of Kubota, Kubo, et al. (2021). In other words, all the previous waveform inversion studies suggested a wider subsidence area than ours (i.e., background color of Figure 6). On the other hand, Nakata et al. (2019) compared uniform and heterogeneous fault models using forward simulations with a grid search, and concluded that this event could be well explained as uniform slips over a fault plane as well as 20 km. Kubota, Kubo, et al. (2021) also estimated the single uniform slip fault model with the fault length of 15 km as shown in Figure 6(C). The size of the present back-projection image is consistent with the length of their estimated uniform fault. Note that our back-projection analysis could estimate tsunami source distribution without any a priori constraints of its fault geometry.

As explained in Section 2, the absolute amplitude or the scaling factor C and the VR were calculated as an indication of our performance using the region of amplitude larger than 0.6 (i.e., surrounded by the green line in Figure 6) and the 70 stations of S-net. The estimated absolute amplitude and the VR were 1.67 m and 59.9%, respectively. The maximums of sea-bottom subsidence estimated by previous studies were 1.3 – 2.4 m (Adriano et al., 2018; Gusman et al., 2016; Nakata et al., 2019; Kubota, Kubo, et al., 2021). Even if taking our result to be 70% underestimated into consideration, as explained in Section 3, the back-projection result of this study (i.e., 2.39 m) is consistent well with the estimation by the waveform inversions. The VR value of 59.9% also confirms the good performance of the present back-projection image.

Next, we investigated snapshots in the tsunami back-projection analysis after the origin time (Figure 7, GIF animation can be seen in Movie S1 in Supporting Information). Note that the amplitude of each image was normalized by the maximum ampli-

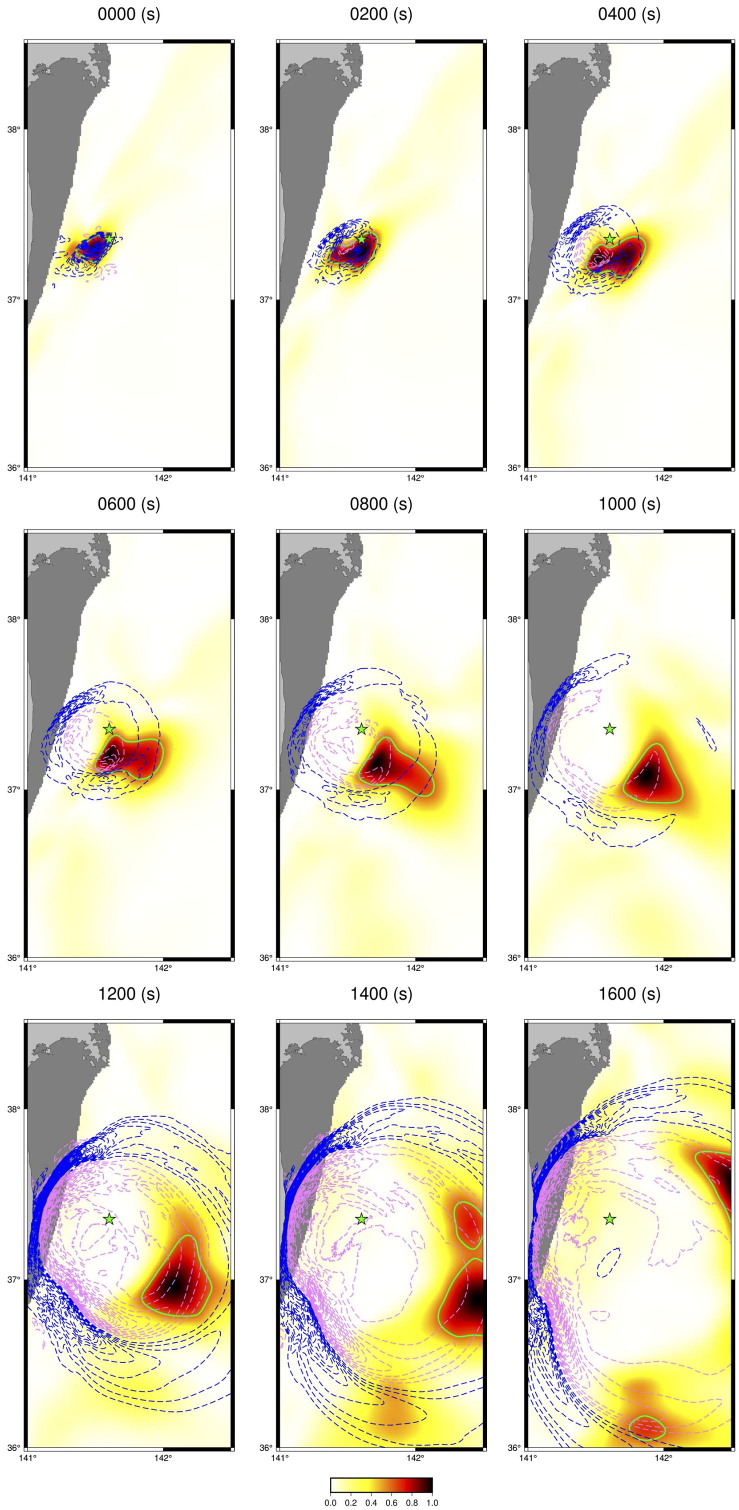

Figure 7. Back-projection images at 0, 200, 400, 600, 800, 1000, 1200, 1400, and 1600 sec after the origin time. The pink and blue contours represent the synthetic tsunamis in positive and negative, respectively, calculated from the initial tsunami height distribution estimated by Kubota, Kubo, et al. (2021). The interval of contours is 0.1 m and 0.02 m at 0 – 1000 sec and at 1200 – 1600 sec, respectively. The green lines represent the area with the back-projected amplitude larger than 0.6. The green star represents the epicenter of the 2016 Off-Fukushima earthquake. Note that the shaded area is shallower than 100 m, so it is not subject to the present analysis.

tude at each time step (Equation (2)), and that the back-projection analysis was applied only to oceanic regions deeper than 100 m. In comparison, the contours of the dashed lines in Figure 7 represent the synthetic sea-surface displacement distribution calculated by the JAGURS code from the initial tsunami height distribution estimated by Kubota, Kubo, et al. (2021). The synthetic tsunami waves propagate of large amplitude mainly in the three directions: northwest, south, and southeast. The northwestern and southern parts are clearly larger than the southeastern, probably due to the bathymetry around the epicenter and the spatial distribution of the assigned tsunami source. On the other hand, the back-projection image of large amplitude moves in the southeast direction, which agrees with the southeastern propagation of the synthetic. In other words, the back-projection analysis detected not only a tsunami source but also some parts of the tsunami propagation, as we have observed in the sinusoidal-wave numerical experiment of Section 3 (Figure 3).

While we can see synthetic tsunami waves propagate in the northwest and south directions in Figure 7, the back-projection image does not show propagations in these two directions. The northwestern part cannot be imaged simply because it is out of the target area of this study. On the other hand, there are no propagations to the south in the image even inside the target area. In Section 7, we will explain why the present tsunami back-projection analysis could not capture this part of propagations, which is related to the specific bathymetry of this study.

6 Applicability for tsunami early warning

As in the case of Figure 6, the locations of the epicenter of an earthquake and its tsunami source are not always same. Our back-projection analysis is suitable to detect such differences compared with tsunami waveform inversions because it dose not require any strong a priori assumptions for imaging. In other words, the back-projection analysis will help tsunami early warning particular for a large event. The larger an earthquake, the broader its tsunami generating area, and the discrepancy in their locations would not be neglected.

The back-projection requires a lot of stations because its main process is to stack coherent waveform data. In this study, we used 70 stations based on the cluster analysis (Section 2). From the point of tsunami early warning views, however, we cannot use all the stations immediately after an earthquake occurs. In this section, we shall investigate the effect of the number of stations on the quality of our back-projection analysis for applicability to tsunami early warning of possible future events.

We first estimated the effect of the number of stations based on theoretical travel times. The numbers of the available stations were 0, 5, 24, 49, 67, and 70, which corresponds to 10, 20, 30, 40, 50, and 60 min after the origin time, respectively. In other words, all the stations used in Section 5 cannot be available until 1 hour after the earthquake in this case. Figure 8 shows how the resulted back-projection image is changed by the number of the adopted stations. There are small amplitudes over the entire target area in the back-projection image at the first 20 min with the small number of stations (Figure 8(A)), but the imaged area is aleardy fairly consistent with the other results at later times or with more stations. Although the number of stations is about one-third of the total, the resulting image at 30 min turns out to be almost identical to the final image presented in Section 5 (Figure 8(B)). After time passes by, calculated at 40 and 50 min, an image gets changed little as the number of stations increases (Figures 8(C) and 8(D)).

In addition, we estimated the absolute amplitude and the VR for each back-projection image. The source area of synthetic waveforms was defined as an amplitude larger than 0.6, as represented in Figure 8(E). Despite of different numbers of stations to be used, all the VR values were defined for the records of all the 70 stations to evaluate the accuracy of the estimated image. The amplitudes of scaling factors were 1.81, 1.83, 1.77, 1.71 m at 20, 30, 40, and 50 min, and their corresponding VRs were 29.9, 50.8, 58.5, and 60.6%. A VR value higher than 50% is generally considered to be reliable (e.g., Kubo et al., 2002), so that the present back-projection analysis can estimate a tsunami source area stably after 30 min of the origin time of the earthquake. In addition, the estimated absolute amplitudes were nearly at all times, so we may say that we could estimate a tsunami size just after 20 min of the origin time.

Lastly, we evaluated the back-projection results from the perspectives of the blind zone and the warning time. The blind zone means the place where no alerts are possible because a tsunami arrives faster than obtaining reliable estimation. The warning time is the time between the detection of the tsunami source and the tsunami arrival (e.g., Allen & Melgar, 2019). Considering the reliable estimation can be obtained after 30 min, because the red stations in Figure 8 represent the arrival of tsunami waves, the blind zone

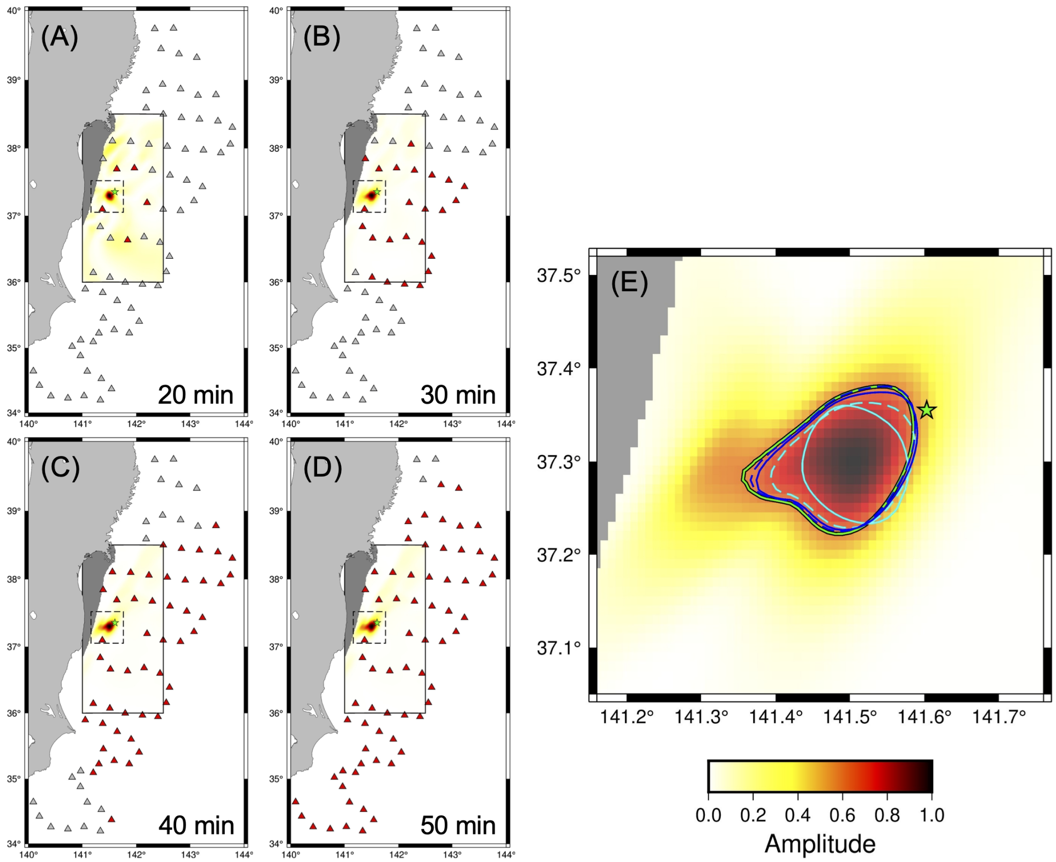

Figure 8. (A) Back-projection image at $t = 0$ by stations available 20 min after the origin time. The red and gray triangles are the stations that can be used at 20 min and all the stations used in Section 5, respectively. The green star represents the epicenter of the 2016 Off-Fukushima earthquake. The black solid line represents the target area of the back-projection image, and the dashed line corresponds to an enlarged area of (E). (B)(C)(D) Same as (A) except that the lapse times are 30, 40, and 50 min. (E) The cyan solid, cyan dashed, blue solid, and blue dashed lines represent the regions of the back-projection image of amplitude larger than 0.6 at 20, 30, 40, and 50 min after the origin time. The background color and the green solid line are the results with all the 70 stations, i.e., the same as Figure 6.

of tsunami early warning, in this case, is limited to only around 37N° (i.e., Fukushima prefecture), very close to the epicenter. Figure 8 also shows the warning times for regions farther than 38.5N° in the north and 35° in the south are longer than 10 min. Actual tsunami amplitudes larger than 50 cm were observed at tidal gauges in the coast from Oarai (located at 36.3N°) to Kuji (located at 40N°) (Gusman et al., 2017). That is, our back-projection analysis could virtually work out as a tsunami early warning for the regions before the tsunamis of this earthquake actually arrived there.

7 Discussion

In this section, we will discuss three topics of the present back-projection analysis: (1) what the tsunami back-projection image actually represents, (2) its applicability for tsunami early warnings of other possible earthquakes, and (3) the difference between the back-projection analysis and the conventional waveform inversion.

First, let us investigate what physical phenomena the tsunami back-projection image reflects. In Figure 6, the back-projection image with amplitude larger than 0.6 agrees very well with the main part of the initial tsunami height distribution estimated by Kubota, Kubo, et al. (2021) (Figure 6). The following temporal sequence of images is consistent with an early part of synthetic tsunami propagations (Figure 7). As pointed out in Section 5, however, the back-projection image did not simulate the tsunami component propagating in the south direction. In the present analysis, we took into account only the direct wave or the path of the minimum travel time from the source to a given station. In other words, the waves reflected once or more at coasts could not be stacked coherently. The southwards propagating waves appear to be refracted by the strong velocity gradient or bathymetry change in the Japan trench, then the propagation direction quickly and abruptly changes towards the coastline where the reflection appears take place (1200 – 1400 sec in Figure 7). This is why the back-projection image of this study could not reproduce the tsunami waves propagating to the south. If tsunami records were stacked with very accurate theoretical travel times of the reflected waves, the propagation to the south might be imaged.

In earthquake source imaging, Kiser et al. (2011) applied the back-projection analysis to multiple seismic phase data in order to enhance its resolution because of wide coverage of take-off angels of waves from the source. In the tsunami case, the use of reflected waves might improve the resulted image. It should be, however, very difficult because small-scale bathymetry data of at least hundreds of meters would be required (e.g., Gusman et al., 2017). Moreover, the effect of nonlinearity cannot be ignored at shallow depth near the coast as well as for an earthquake larger than $M_w 8.0$ (Kubota, Saito, et al., 2018). These factors should be carefully investigated in future in order to upgrade back-projection approaches.

We now consider why our back-projection images reflect not only a tsunami excitation area but also an early stage of tsunami propagations. Back-projection analyses have been widely applied to seismic records, and their results were considered to be the radiated energy on an actual fault (e.g., Ishii et al., 2007). Seismic waves, P waves in most cases, immediately propagate away from the fault in a 3-D manner as shown in Figure 3(D). In the case of tsunamis, on the other hand, the target area is the whole sea surface which contains not only the tsunami source but also propagation paths and stations. As a result, the back-projection analysis using tsunami waveforms can estimate both sources and an early part of the propagation processes of tsunamis.

Next, let us discuss the applicability of the tsunami back-projection analysis to tsunami early warning.

In this study, we set $t = 0$ of the back-projection analysis to be the earthquake origin time, which was estimated by JMA using seismic records (Section 2). Since the seismic wave speed is faster than the tsunami one, it can be obtained before the back-projection analysis. In the case of larger earthquakes, however, the tsunami origin time would be different from the earthquake one. For example, in the 2011 Tohoku earthquake case, Satake et al. (2013) found that the huge shallow slip or sea-bottom displacement occurred 3 min after the origin time. In such cases, the back-projection image for the actual tsunami source would be $t > 0$ instead of $t = 0$. However, because we applied the filter forward and backward in time and used the time window of 300 sec in the final step of the back-projection analysis (Equation 2), there is little difference in the back-projection image between before the tsunami origin time and the actual one (Figure S1 in Supporting Information).

From the result in Section 6, the back-projection image of the event of this study provides reliable information about the tsunami source distribution at 30 min after the origin time. The VR of images increases in time, as explained in Section 6 and Figure

8, but it was dropped to 59.9% at the final 60 min. This may be due to the poor quality of waveforms or weak tsunami signals at the stations added in the last final 10 minutes because each OBPG waveform was weighted equally (i.e., each record was normalized) in the present analysis (Section 2). Nevertheless, the back-projection images at later time steps agreed very well with each other (Figure 8), which guarantees a stable result regardless of a detailed selection of the stations to be used.

Considering how to select stations used in the analysis may be important for other tsunami-exciting earthquakes. In this study, we selected the stations by the cluster analysis for the coherency of records, as explained in Section 2, so let us investigate how such a cluster was formed. Figure 9(A) shows the ray paths calculated by the ray-tracing method proposed by Satake (1988) with a 1° interval, that is, solving the ray tracing equations by the Runge-Kutta method. Hereafter, each cluster will be referred to the colors shown in Figure 1(A) (e.g., the largest cluster is called the "red cluster"). In figure 9(A), rays directly reach all the stations of the red cluster but not stations of other clusters.

Figure 9(B) compares waveforms of each cluster normalized of 1200 sec in record length before and after each theoretical travel time. The farther a station from the red cluster, the more the tsunami wave arrival is delayed for the other clusters. Moreover, a waveform becomes smoother at a farther station, that is, high-frequency components decay. This is known as the diffraction phenomenon of waves where waves propagate into regions of a geometrical shadow or no geometrical rays, as investigated in detail in seismology (e.g., Chapman & Orcutt, 1985; Aki & Richards, 2002). A significant shadow zone of tsunamis in the S-net region is formed by the refraction due to the sudden bathymetry change near the Japan trench (Figure 9(A)). Stations of the green, purple, and cyan clusters are located within a shadow zone of tsunami waves, and their varied waveforms appear to degrade the resulted back-projection image.

The spatial resolution distribution in Figures 5(B) and Figures 5(C) can be also explained by the tsunami diffraction because the grids of large ratios are located along the Japan trench (Figure 5(A)).

Recent seismic back-proejections combine multiple arrays to improve their estimations (e.g., Kiser & Ishii, 2012; Xie & Meng, 2020). In the present tsunami back-projection analysis, however, combining several clusters should be difficult because of the incoherence of waveforms for clusters affected by the above effect.

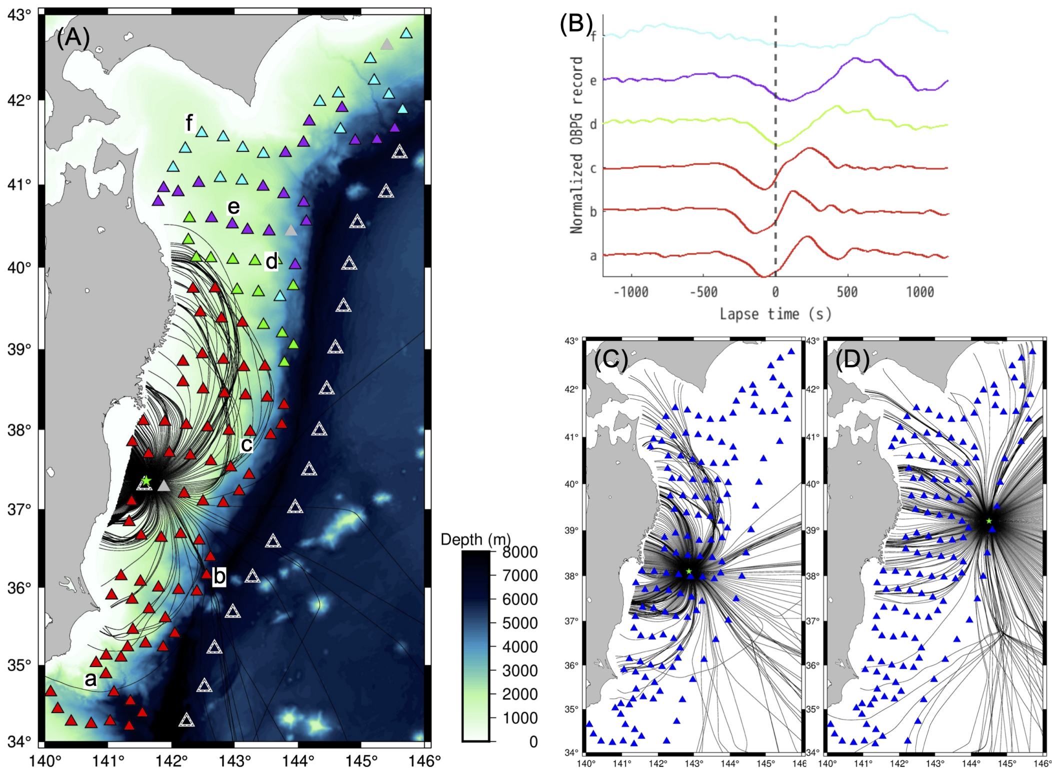

Figure 9. The calculation results of tsunami ray paths with a 1° interval in each earthquake. (A) The triangles and green star are S-net stations and the epicenter of the 2016 Off-Fukushima earthquake, i.e., the same as Figure 1(A). The black lines are the ray paths from the epicenter, and the background color represents bathymetry. (B) The records of S-net OBPGs applied by the band-pass filter of 100–3000 sec. Each waveform is plotted 1200 sec before and after each theoretical travel time (i.e., lapse time 0 means the theoretical travel time). The station names, a, b, c, d, e, and f are shown in (A), and the color of each waveform is the same as the color of the cluster that the station belongs to. (C) Same as (A) except for the 2011 Tohoku-Oki earthquake. Blue triangles are the S-net stations and the green star is the source of the rays. (D) Same as (C) except for the 1933 Off-Sanriku earthquake.

If the clustering of stations is due to the effect of tsunami diffraction, the number of available stations in the back-projection analysis should depend on a source location. Figures 9(C) and 9(D) compare ray paths of other two types of earthquakes in the Japan trench subduction zone and its outer rise region. They correspond to the epicenters of the 2011 Tohoku-Oki earhquake (e.g., Satake et al., 2013) and the 1933 Off-Sanriku earthquake (e.g., Kanamori, 1971), respectively. The further a source is located away from the coast of Japan, the more S-net stations geometrical rays can reach. While stations in the northeast and the southwest are located in the shadow zone for the subduction event (Figure 9(C)), rays arrive at all the S-net stations for the outer rise one (Figure 9(D)), that is, we are expected to use all the stations in the back-projection analysis, which probably leads to better results than the present case located near the coast. Because a ray of tsunamis is determined by the bathymetry, we can select useful stations for each event beforehand, depending on its location, for tsunami early warning.

The degree of resemblance among waveforms leads to clustering. Figure 4 in Section 3 investigated the effect of a source with both positive and negative poralities (i.e., uplift and subsidence). It shows that a simple stacking of records with a high correlation coefficient may lead to not only better but also worse images. The clustering analysis and the ray tracing should be important in such a case to group appropriate stations for the back-projection analysis.

As the final topic, let us compare the back-projection analysis with a widely used waveform inversion approach.

Tsunami waveform inversion studies require strong constraints on the target area based on other kinds of studies such as CMT and fault geometry estimated by seismic or geodetic data (e.g., Piatanesi & Lorito, 2007; Fujii et al., 2011; Gusman et al., 2017). In contrast, the single a priori information of the back-projection method is a gross source location area. For example, in the tsunami waveform inversion of the present earthquake, Gusman et al. (2017) used 4×3 subfaults sized of 10 km $\times$ 10 km, and Kubota, Kubo, et al. (2021) used tsunami sources in an area of 50 km $\times$ 50 km distributed with 2 km intervals. The present back-projection analysis could cover a very broad area in longitude between 141E° and 142.5E° and in latitude between 36N° and 38.5° with the grid spacing as small as 0.01° or about 1 km (Section 2). The spatial resolution of the tsunami source was found to be about 10 km and 2 km in x- and y-direction, respectively, as shown in Figure 5. In other words, the back-projection analysis could search for a wider area of higher resolution, especially in the y or north-south direction than a waveform inversion case. Note that even the 10 km resolution in the x or east-west direction is enough to estimate the source size of this event (M_w6.9). In addition, the back-projection analysis does not need artificial constrains such as non-negative and smooth source distributions, or better to say, the analyzed data naturally lead to their possible resolution in image.

The size of the back-projection image turned out to be narrower than those of previous waveform inversion studies (Section 5). One of the interesting problems of this event is that the fault lengths estimated by the grid search were shorter than the ones of the waveform inversions. Nakata et al. (2019) and Kubota, Kubo, et al. (2021) conducted grid-searches with the uniform single fault slip, and both found that the observed tsunamis could be explained by a fault of about 15 – 20 km long. This fault length was about half the estimation from the standard earthquake scaling law (e.g., Utsu, 2001). Kubota, Kubo, et al. (2021) adopted a different multiple fault model, and concluded that the length of the main rupture area might be about 35 km. In contrast, our back-projection image is consistent well with the single-fault model (Figure 6). As discussed above, our back-projection analysis can distinguish images on such a scale, so it indicates that the fault size of this earthquake was likely to be smaller than the scaling relation, that is, 15 – 20 km long. In other words, our back-projection analysis revealed a new feature of the 2016 Off-Fukushima earthquake, that is, the slip amount was twice and the fault size was half the standard earthquake of its magnitude.

Although the tsunami back-projection analysis has many advantages, we may point out some disadvantages. When a tsunami wavelength is not much longer than ocean depth, the dispersive effect cannot be ignored. In such a case, the waveforms are expected to vary in propagation distance, which would degrade the coherency among stations. Although a waveform inversion method can include the effect of dispersion in the Green's functions (Saito et al., 2010), calculating dispersive Green's functions takes much more computational cost than a non-dispersive case because of iterative solving procedures for linear dispersive equations (e.g., Saito, 2019). Nevertheless, this effect may not be critical especially for tsunami early warning because the wavelength of large tsunamis which cause huge damage in coastal areas is generally long enough for the linear long-wave approximation. For tsunamis excited by an event very far from an array, on the other hand, tsunami waveforms also show dispersive characters in a very long period range (Watada et al., 2014). However, this type of dispersions may not be critical because the data were filtered by 100 – 3000 sec in the present analysis (Section 2). Since the tsunami propagation distance was less than 500 km and the average sea depth of stations is about 2 km, the dispersive effect may appear in the period range of only less than 90 sec, at least in the present case.

8 Conclusions

We applied the back-projection analysis to the S-net OBPG records associated with the 2016 Off-Fukushima earthquake. The estimated back-projection image reflected the initial tsunami or sea-surface height distribution near the epicenter. In addition, we could estimate the absolute amplitude of the source base on the scaling factor estimaion of Hossen et al. (2015), and the result (1.67 m in the maximum) agreed well with the previous stuides using waveform inversion methods (1.3 – 2.4 m). The tsunami back-projection analysis imaged not only the original tsunami source but also an early part of tsunami propagations. This is because the target area of the analysis is the whole sea surface including the source area, propagation paths, and stations (Figure 3(D)).

Due to the high spatial resolution of the back-projection analysis, it was confirmed that the fault size of this earthquake was smaller than the standard scaling law. This has been speculated in previous studies, but not emphasized strongly because it was inconsistent with results of several waveform inversions. Our result therefore assists the understanding of the mechanism of intraplate earthquakes such as the 2016 Off-Fukushima earthquake.

We also investigated the applicability of the back-projection analysis to tsunami early warning. In the present case, the back-projection analysis yielded reliable results 30 min after the origin time. The number of available stations in the analysis, however, depends on the source location. The refraction of tsunamis in the Japan trench makes clear shadow zones, and the observed waveforms passing by such zones should be transformed because of the diffraction effect there. The essence of the back-projection analysis is stacking coherent waveforms, so that the presence of shadow zones limits the number of available stations. Megathrust or outer rise earthquakes near a trench axis, in contrast to the present one near the coast in a shallow ocean, appear to yield smaller or no shadow zones (Figure 9). In addition, now we can use the records of outer trench stations of the S-net, i.e., the number and the configuration of available stations have been already enhanced. The above disadvantage therefore should not be so critical in practice now.

In the case of a large earthquake, the tsunami source may have both positive and negative regions. As shown in Section 3, the polarity correction makes the resulted image worse in the case of such dipole displacements, that is, it seems to be overcorrected, although further studies with real data should be needed. At present, we consider that the polarity correction is not required because the location and intensity of a tsunami source can be grossly estimated.

The advantage of the back-projection is its simplicity. We can estimate the tsunami excitation area without any special a priori information or much computational cost. Recently, meteorological tsunamis excited by atmospheric pressure changes were clearly observed in S-net (Saito et al., 2021; Kubota, Saito, et al., 2021). Because the general scale of the atmospheric pressure changes is large, the back-projection analysis may be useful to detect such events as moving sources or images changing in time as for the seismic back-projection analysis.

In addition, the tsunami back-projection will be useful to tsunami early warning as for the following reasons:

1. It does not require any specific a priori information about a source. It will be therefore useful when the locations of the epicenter and the tsunami source are clearly different, as in our example shown in Figure 6. Such discrepancy would be more important for larger events as well as tsunami earthquakes.
2. It can estimate a broad area with a margin for the search of the source location without compromising results. It will therefore provide waveform inversions with an appropriate target area (e.g., it can be used instead of an ”influence area” of Tsushima et al. (2012)).
3. It can estimate an early part of propagation characteristics of tsunamis directly, so that we may detect the directivity of tsunamis as estimated by data assimilation approaches (e.g., Maeda et al., 2015; Hoshiba & Aoki, 2015).

4. It will enhance the reliability of tsunami source estimations because of its independence of the other existing methods such as a waveform inversion or a grid search estimation.

OBPG arrays now have been available around the world, so that the back-projection analysis will be one of the useful techniques for not only seismic waves but also tsunamis.

Availability statement

The S-net OBPG data (National Research Institute for Earth Science and Disaster Resilience [NIED], 2019) can be downloaded from the NIED website (`https://www.seafloor.bosai.go.jp`, in Japanese) with data request and permission. The JAGURS code (Baba et al., 2016) used to calculate synthetic tsunamis can be downloaded from GitHub (`https://github.com/jagurs-admin/jagurs`). The tsunami source model of Kubota, Kubo, et al. (2021) is available in the Supporting Information of that paper, and the slip distribution models of Gusman et al. (2017),Adriano et al. (2018), and Nakata et al. (2019) are available in each paper. The tsunami source image estimated by the back-projection analysis is available the in Supporting information of this paper.

Acknowledgments

We thank NIED for providing the records of OBPG. Tatsuya Kubota kindly pointed out their tsunami source models with S-net data. We also thank the editor, Ryan Mulligan, and three anonymous reviewers for their constructive comments.

References

Adriano, B., Fujii, Y., & Koshimura, S. (2018, December). Tsunami source and inundation features around Sendai Coast, Japan, due to the November 22, 2016 Mw 6.9 Fukushima earthquake. *Geoscience Letters*, *5*(1), 2.

Aki, K., & Richards, P. G. (2002). *Quantitative seismology* (2nd ed.). University Science Books.

Allen, R. M., & Melgar, D. (2019). Earthquake Early Warning: Advances, Scientific Challenges, and Societal Needs. *Annual Review of Earth and Planetary Sciences*, *47*(1), 361–388. doi: 10.1146/annurev-earth-053018-060457

Amante, C., & Eakins, B. W. (2009). *ETOPO1 Global Relief Model con-*

verted to PanMap layer format [data set]. PANGAEA. doi: 10.1594/PANGAEA.769615

An, C., & Meng, L. (2017). Time reversal imaging of the 2015 Illapel tsunami source. *Geophysical Research Letters*, *44*(4), 1732–1739. doi: 10.1002/2016GL071304

Aoi, S., Asano, Y., Kunugi, T., Kimura, T., Uehira, K., Takahashi, N., ... Fujiwara, H. (2020). MOWLAS: NIED observation network for earthquake, tsunami and volcano. *Earth, Planets and Space*, *72*(1), 126. doi: 10.1186/s40623-020-01250-x

Baba, T., Ando, K., Matsuoka, D., Hyodo, M., Hori, T., Takahashi, N., ... Saka, R. (2016). Large-scale, high-speed tsunami prediction for the Great Nankai Trough Earthquake on the K computer. *The International Journal of High Performance Computing Applications*, *30*(1), 71–84. doi: 10.1177/1094342015584090

Chapman, C. H., & Orcutt, J. A. (1985). The computation of body wave synthetic seismograms in laterally homogeneous media. *Reviews of Geophysics*, *23*(2), 105–163. doi: 10.1029/RG023i002p00105

Fujii, Y., Satake, K., Sakai, S., Shinohara, M., & Kanazawa, T. (2011). Tsunami source of the 2011 off the Pacific coast of Tohoku Earthquake. *Earth, Planets and Space*, *63*(7), 815–820. doi: 10.5047/eps.2011.06.010

Fukahata, Y., Yagi, Y., & Rivera, L. (2014). Theoretical relationship between back-projection imaging and classical linear inverse solutions. *Geophysical Journal International*, *196*(1), 552–559.

Fukao, Y., Sandanbata, O., Sugioka, H., Ito, A., Shiobara, H., Watada, S., & Satake, K. (2018). Mechanism of the 2015 volcanic tsunami earthquake near Torishima, Japan. *Science Advances*, *4*(4), eaao0219. doi: 10.1126/sciadv.aao0219

Gusman, A. R., Satake, K., Shinohara, M., Sakai, S., & Tanioka, Y. (2017). Fault Slip Distribution of the 2016 Fukushima Earthquake Estimated from Tsunami Waveforms. *Pure and Applied Geophysics*, *174*(8), 2925–2943.

Gusman, A. R., Sheehan, A. F., Satake, K., Heidarzadeh, M., Mulia, I. E., & Maeda, T. (2016). Tsunami data assimilation of Cascadia seafloor pressure gauge records from the 2012 Haida Gwaii earthquake. *Geophysical Research Letters*, *43*(9), 4189–4196. doi: 10.1002/2016GL068368

Hoshiba, M., & Aoki, S. (2015). Numerical Shake Prediction for Earthquake Early Warning: Data Assimilation, Real-Time Shake Mapping, and Simulation of Wave Propagation. *Bulletin of the Seismological Society of America*, *105*(3), 1324–1338. doi: 10.1785/0120140280

Hossen, M. J., Cummins, P. R., Roberts, S. G., & Allgeyer, S. (2015). Time Reversal Imaging of the Tsunami Source. *Pure and Applied Geophysics*, *172*(3-4), 969–984. doi: 10.1007/s00024-014-1014-5

Ishii, M., Shearer, P. M., Houston, H., & Vidale, J. E. (2005). Extent, duration and speed of the 2004 Sumatra–Andaman earthquake imaged by the Hi-Net array. *Nature*, *435*(7044), 933–936.

Ishii, M., Shearer, P. M., Houston, H., & Vidale, J. E. (2007). Teleseismic *P* wave imaging of the 26 December 2004 Sumatra-Andaman and 28 March 2005 Sumatra earthquake ruptures using the Hi-net array. *Journal of Geophysical Research*, *112*(B11), B11307.

Kanamori, H. (1971). Seismological evidence for a lithospheric normal faulting — the Sanriku earthquake of 1933. *Physics of the Earth and Planetary Interiors*, *4*(4), 289–300. doi: 10.1016/0031-9201(71)90013-6

Kiser, E., & Ishii, M. (2012). Combining seismic arrays to image the high-frequency characteristics of large earthquakes: Seismic arrays to image large earthquakes. *Geophysical Journal International*, *188*(3), 1117–1128. doi: 10.1111/j.1365-246X.2011.05299.x

Kiser, E., & Ishii, M. (2017). Back-Projection Imaging of Earthquakes. *Annual Review of Earth and Planetary Sciences*, *45*(1), 271–299.

Kiser, E., Ishii, M., Langmuir, C. H., Shearer, P. M., & Hirose, H. (2011). Insights into the mechanism of intermediate-depth earthquakes from source properties as imaged by back projection of multiple seismic phases. *Journal of Geophysical Research: Solid Earth*, *116*(B6). doi: 10.1029/2010JB007831

Kohler, M. D., Bowden, D. C., Ampuero, J., & Shi, J. (2020). Globally Scattered 2011 Tohoku Tsunami Waves From a Seafloor Sensor Array in the Northeast Pacific Ocean. *Journal of Geophysical Research: Solid Earth*, *125*(11). doi: 10.1029/2020JB020221

Kubo, A., Fukuyama, E., Kawai, H., & Nonomura, K. (2002). NIED seismic moment tensor catalogue for regional earthquakes around Japan: quality test and application. *Tectonophysics*, *356*(1), 23–48. doi: 10.1016/S0040-1951(02)00375-X

Kubota, T., Kubo, H., Yoshida, K., Chikasada, N. Y., Suzuki, W., Nakamura, T., & Tsushima, H. (2021). Improving the Constraint on the M_{W} 7.1 2016 Off-Fukushima Shallow Normal-Faulting Earthquake With the High Azimuthal Coverage Tsunami Data From the S-net Wide and Dense Network: Implication for the Stress Regime in the Tohoku Overriding Plate. *Journal of Geophysical Research: Solid Earth*, *126*(10). doi: 10.1029/2021JB022223

Kubota, T., Saito, T., Chikasada, N. Y., & Sandanbata, O. (2021). Meteotsunami Observed by the Deep-Ocean Seafloor Pressure Gauge Network Off Northeastern Japan. *Geophysical Research Letters*, *48*(21), e2021GL094255. doi: 10.1029/2021GL094255

Kubota, T., Saito, T., Ito, Y., Kaneko, Y., Wallace, L. M., Suzuki, S., … Henrys, S. (2018). Using Tsunami Waves Reflected at the Coast to Improve Offshore Earthquake Source Parameters: Application to the 2016 Mw 7.1 Te Araroa Earthquake, New Zealand. *Journal of Geophysical Research: Solid Earth*, *123*(10), 8767–8779. doi: 10.1029/2018JB015832

Kubota, T., Suzuki, W., Nakamura, T., Chikasada, N. Y., Aoi, S., Takahashi, N., & Hino, R. (2018). Tsunami source inversion using time-derivative waveform of offshore pressure records to reduce effects of non-tsunami components. *Geophysical Journal International*, *215*(2), 1200–1214. doi: 10.1093/gji/ggy345

Larmat, C., Montagner, J.-P., Fink, M., Capdeville, Y., Tourin, A., & Clévédé, E. (2006). Time-reversal imaging of seismic sources and application to the great Sumatra earthquake. *Geophysical Research Letters*, *33*(19). doi: 10.1029/2006GL026336

Lin, F.-C., Kohler, M. D., Lynett, P., Ayca, A., & Weeraratne, D. S. (2015, May). The 11 March 2011 Tohoku tsunami wavefront mapping across offshore Southern California. *Journal of Geophysical Research: Solid Earth*, *120*(5), 3350–3362. doi: 10.1002/2014JB011524

Maeda, T., Obara, K., Shinohara, M., Kanazawa, T., & Uehira, K. (2015). Successive estimation of a tsunami wavefield without earthquake source data: A data assimilation approach toward real-time tsunami forecasting. *Geophysical Research Letters*, *42*(19), 7923–7932. doi: 10.1002/2015GL065588

Matsumoto, K., Takanezawa, T., & Ooe, M. (2000). Ocean Tide Models Developed by Assimilating TOPEX/POSEIDON Altimeter Data into Hydrodynamical Model: A Global Model and a Regional Model around Japan. *Journal of Oceanography*, *56*(5), 567–581. doi: 10.1023/A:1011157212596

Mizutani, A., Yomogida, K., & Tanioka, Y. (2020). Early Tsunami Detection With Near-Fault Ocean-Bottom Pressure Gauge Records Based on the Comparison With Seismic Data. *Journal of Geophysical Research: Oceans*, *125*(9), e2020JC016275. doi: 10.1029/2020JC016275

Nakata, K., Hayashi, Y., Tsushima, H., Fujita, K., Yoshida, Y., & Katsumata, A. (2019). Performance of uniform and heterogeneous slip distributions for the modeling of the November 2016 off Fukushima earthquake and tsunami, Japan. *Earth, Planets and Space*, *71*(1), 30.

National Research Institute for Earth Science and Disaster Resilience [NIED]. (2019). NIED S-net. *National Research Institute for Earth Science and Disaster Resilience*. doi: https://doi.org/10.17598/nied.0007

Piatanesi, A., & Lorito, S. (2007). Rupture Process of the 2004 Sumatra–Andaman Earthquake from Tsunami Waveform Inversion. *Bulletin of the Seismological Society of America*, *97*(1A), S223–S231. doi: 10.1785/0120050627

Romesburg, C. (2004). *Cluster Analysis for Researchers*. Lulu.com.

Saito, T. (2019). *Tsunami Generation and Propagation*. Springer Geophysics.

Saito, T., Kubota, T., Chikasada, N. Y., Tanaka, Y., & Sandanbata, O. (2021). Meteorological Tsunami Generation Due to Sea-Surface Pressure Change: Three-Dimensional Theory and Synthetics of Ocean-Bottom Pressure Change. *Journal of Geophysical Research: Oceans*, *126*(5). doi: 10.1029/2020JC017011

Saito, T., Satake, K., & Furumura, T. (2010). Tsunami waveform inversion including dispersive waves: the 2004 earthquake off Kii Peninsula, Japan. *Journal of Geophysical Research: Solid Earth*, *115*(B6). doi: 10.1029/2009JB006884

Saito, T., & Tsushima, H. (2016). Synthesizing ocean bottom pressure records including seismic wave and tsunami contributions: Toward realistic tests of monitoring systems. *Journal of Geophysical Research: Solid Earth*, *121*(11), 8175–8195. doi: 10.1002/2016JB013195

Satake, K. (1987). Inversion of tsunami waveforms for the estimation of a fault heterogeneity: Method and numerical experiments. *Journal of Physics of the*

Earth, *35*(3), 241–254.

Satake, K. (1988). Effects of bathymetry on tsunami propagation: Application of ray tracing to tsunamis. *Pure and Applied Geophysics*, *126*(1), 27–36.

Satake, K., Fujii, Y., Harada, T., & Namegaya, Y. (2013). Time and Space Distribution of Coseismic Slip of the 2011 Tohoku Earthquake as Inferred from Tsunami Waveform Data. *Bulletin of the Seismological Society of America*, *103*(2B), 1473–1492. doi: 10.1785/0120120122

Sethian, J. (1999). *Level Set Methods and Fast Marching Methods* (2nd ed.). Cambridge Unversity Press.

Tsushima, H., Hino, R., Tanioka, Y., Imamura, F., & Fujimoto, H. (2012). Tsunami waveform inversion incorporating permanent seafloor deformation and its application to tsunami forecasting. *Journal of Geophysical Research: Solid Earth*, *117*(B3).

Utsu, T. (2001). *Seismology* (3rd ed.). Kyoritsu Shuppan. (in Japanese)

Wang, Y., & Satake, K. (2021). Real-Time Tsunami Data Assimilation of S-Net Pressure Gauge Records during the 2016 Fukushima Earthquake. *Seismological Research Letters*, *92*(4), 2145–2155. doi: 10.1785/0220200447

Watada, S., Kusumoto, S., & Satake, K. (2014). Traveltime delay and initial phase reversal of distant tsunamis coupled with the self-gravitating elastic Earth: DELAY AND PRECURSOR OF DISTANT TSUNAMI. *Journal of Geophysical Research: Solid Earth*, *119*(5), 4287–4310. doi: 10.1002/2013JB010841

Xie, Y., & Meng, L. (2020). A Multi-Array Back-Projection Approach for Tsunami Warning. *Geophysical Research Letters*, *47*(14), e2019GL085763. Retrieved 2022-04-24, from `https://onlinelibrary.wiley.com/doi/abs/10.1029/2019GL085763` doi: 10.1029/2019GL085763

Yagi, Y., Nakao, A., & Kasahara, A. (2012). Smooth and rapid slip near the Japan Trench during the 2011 Tohoku-oki earthquake revealed by a hybrid back-projection method. *Earth and Planetary Science Letters*, *355-356*, 94–101.